The Canadian Mineralogist
Vol. 42, pp. 1405-1424 (2004)

PHYSICAL CONDITIONS OF GOLD DEPOSITION AT THE McPHEES DEPOSIT, PILBARA CRATON, WESTERN AUSTRALIA: FLUID INCLUSION AND STABLE ISOTOPE CONSTRAINTS

DARCY E.L. BAKER[§] AND PHILIP K. SECCOMBE

Tectonics and Earth Resources Research Group, The University of Newcastle, Callaghan, NSW 2308, Australia

ABSTRACT

Fluid inclusions in mineralized quartz veins from the *ca.* 2890 Ma McPhees gold deposit, Pilbara Craton, Western Australia, were examined to determine the composition of the mineralizing fluid and to constrain the physical conditions of gold deposition. The composition of inclusions was determined by standard microthermometric and laser Raman analyses of selected assemblages of fluid inclusions. The veins contain: (1) abundant, Type-Ia monophase, CO_2-rich inclusions and coeval Type-Ib two-phase, mixed $H_2O + CO_2$ inclusions; (2) secondary, two-phase, Types II and III, respectively, low- and high-salinity aqueous inclusions, and (3) secondary Type-IV monophase, mixed CO_2–CH_4–N_2 inclusions. Type-Ib inclusions have highly variable bulk-compositions (10–100 vol.% CO_2–CH_4) and variable salinity (3–12 eq. wt.% NaCl). Types II and III inclusions have similar morphologies and modes of occurrence, but have distinctly different salinities (0.3–12.6 eq. wt.% and >21.0 eq. wt.%, respectively). Heating experiments indicate minimum temperatures of trapping of 350 ± 641°C for Type-I inclusions, 207 ± 660°C for Type-II inclusions, and 143 ± 637°C for Type-III inclusions. Oxygen isotope compositions of quartz–actinolite and albite–actinolite pairs indicate a temperature of gold-associated alteration of ~350°C, consistent with arsenopyrite thermometry, which indicates gold mineralization at <480°C. The early CO_2-rich fluid inclusions have densities that range from 0.6 to 1.05 g/cm^3 which, at 350°C, correspond to 1–2 kbar pressure, consistent with geological relations indicating that the McPhees deposit formed at <7 km. Type-I inclusions are interpreted to contain early vein-related fluids that carried gold, but this assemblage (nearly pure CO_2 and subordinate, coexisting H_2O-rich fluid inclusions) is unusual for orogenic gold deposits. It is most likely a result of fluid mixing that may have played a role in gold deposition in veins; however, host-rock lithology seems to have been a first-order control in localizing the gold.

Keywords: orogenic gold deposit, McPhees deposit, CO_2-rich fluid inclusions, oxygen isotopes, fluid mixing, Pilbara Craton, Archean, Australia.

SOMMAIRE

Nous avons examiné les inclusions fluides piégées dans le quartz de veines minéralisées du gisement aurifère de McPhees, formé il y a environ 2890 millions d'années, au craton de Pilbara, en Australie occidentale, afin de déterminer la composition du fluide minéralisateur et de délimiter les conditions physiques de déposition de l'or. Nous avons déterminé la composition des inclusions par analyses microthermométriques conventionnelles et par analyses Raman au laser d'assemblages choisis d'inclusions fluides. Les veines contiennent: (1) une abondance d'inclusions dites de type Ia, monophasées, à CO_2, et de type Ib, contemporaines, à deux phases, $H_2O + CO_2$; (2) des inclusions aqueuses secondaires à deux phases, à faible (type II) ou à forte salinité (type III), et (3) des inclusions secondaires monophasées, de type IV, contenant un mélange CO_2–CH_4–N_2. Les inclusions de type Ib ont une composition très variable (10–100 vol.% CO_2–CH_4) et une salinité variable (3–12% equivalents de NaCl). Les inclusions de types II et III adoptent une morphologie et un mode de distribution semblables, mais avec des salinités distinctes (0.3–12.6% et >21.0% équivalents de NaCl, respectivement). Des expériences de chauffage indiquent une température de piégeage minimale de 350 ± 641°C pour les inclusions de type I, 207 ± 660°C pour celles de type II, et 143 ± 637°C pour celles de type III. Les compositions isotopiques de l'oxygène des assemblages quartz + actinolite et albite + actinolite indiquent une température d'altération accompagnant la minéralisation aurifère d'environ 350°C, ce qui concorde avec les résultats de la géothermométrie fondée sur l'arsénopyrite, qui indique une minéralisation à environ 480°C. La phase fluide carbonatée précoce avait une densité entre 0.6 et 1.05 g/cm^3, ce qui, à 350°C, correspond à une pression entre 1 et 2 kbar. Les relations de terrain indiquent une profondeur du gisement d'environ 7 km. Les inclusions de type I semblent échantillonner la phase fluide précoce porteuse d'or, circulant dans le système de veines, mais cet assemblage (inclusions de CO_2 presque pur et inclusions moins importantes de fluide

§ *Current address*: Equity Engineering Ltd., 700–700 West Pender Street, Vancouver, British Columbia V6C 1G8, Canada. *E-mail address*: darcyb@equityeng.bc.ca

aqueux coexistant) est inhabituel dans les gisements aurifères orogéniques. L'association, qui serait due à un mélange de fluides, pourrait avoir eu une rôle déterminant dans la déposition de l'or dans les veines. Toutefois. il semble clair que la composition des roches hôtes a joué un rôle primordial dans la distribution de l'or.

(Traduit par la Rédaction)

Mots-clés: gisement d'or orogénique, gisement de McPhees, inclusions fluides à CO_2, isotopes d'oxygène, mélange de fluides, craton de Pilbara, archéen, Australie.

Introduction

The early Archean Pilbara Craton, northwestern Australia (Fig. 1a), is endowed with numerous, small gold deposits (typically <10 tonnes Au) hosted by mafic to ultramafic volcanic rocks or sedimentary sequences. These deposits contrast in size with those in other Archean terranes, such as the Superior Province in Canada or the Yilgarn Craton in Australia, which each host numerous world-class gold deposits (Card *et al.* 1989, Hodgson 1993, Robert & Poulsen 1997, Hagemann & Cassidy 2000, Goldfarb *et al.* 2001). Despite geological similarities with these and other Archean terranes, the Pilbara Craton has yielded relatively insignificant amounts of gold. For example, based on the area of greenstone belts, greater than one order of magnitude more gold has been produced in the Yilgarn Craton than in the Pilbara Craton (Groves *et al.* 1990). As such, gold occurrences in the Pilbara Craton have traditionally received little attention, and there are few modern studies of gold mineralization from this region.

Determination of the composition of paleofluids trapped within hydrothermal minerals can provide valuable information on how gold was transported and, in combination with knowledge of the stability of individual included phases, can be used to estimate the P–T conditions of deposition. Independent estimates of T (or

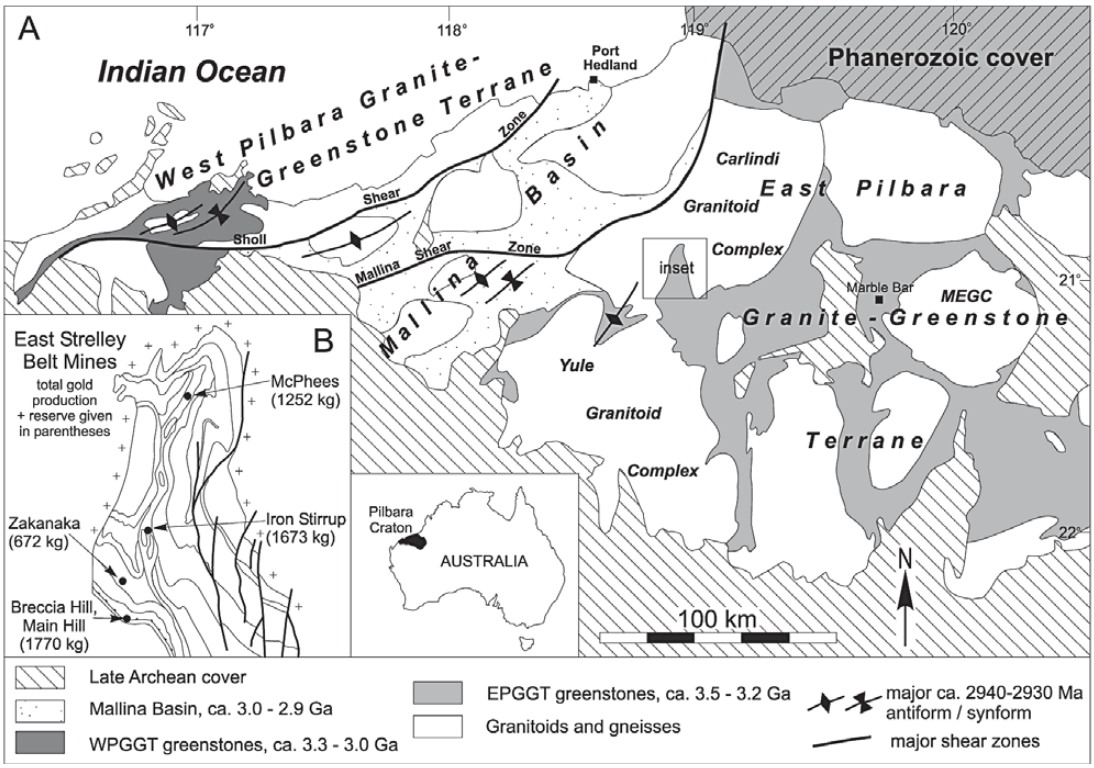

FIG. 1. A. Geological map of the northern Pilbara Craton showing the location of the East Strelley Belt in the central part of the craton. B. Inset showing more detailed view of East Strelley Belt, with locations and gold production + reserves for the main deposits.

P), such as those based on oxygen isotope geothermometry, make a study of fluid inclusions a powerful technique to constrain the physical conditions of gold deposition. Such studies of gold mineralization in the Pilbara Craton have been limited to sediment-hosted lode and epithermal deposits (Blewett *et al.* 2002, Huston *et al.* 2002a) and to preliminary results from the McPhees deposit (Baker & Seccombe 2001, Baker *et al.* 2002). As well, Neumayr (1993) included data on fluid inclusions from the Mount York district, and Huston *et al.* (2001) included reconnaissance data on fluid inclusions from the Warrawoona district. In this paper, we present more complete results from our fluid-inclusion study of the McPhees deposit, hosted by mafic and ultramafic rocks, and integrate these data with oxygen isotopic compositions of hydrothermal minerals (quartz, actinolite and albite) and arsenopyrite compositions to constrain the physical conditions of gold deposition in the central part of the Pilbara Craton.

Geological Setting

The McPhees gold deposit is located within the East Pilbara Granite–Greenstone Terrane (EPPGT, Van Kranendonk *et al.* 2002), which is characterized by a distinctive pattern of large (~30–125 km), ovoid, multiphase bodies of granitic rocks surrounded by arcuate, steeply dipping, narrow greenstone belts. The East Strelley Belt (Fig. 1b; formerly named the Pilgangoora Greenstone Belt) lies in the central region of the Pilbara Craton (Fig. 1), near the western margin of the EPGGT, and hosts the McPhees gold deposit. Hickman (1983), Barley (1993), Krapez (1993) and Van Kranendonk *et al.* (2002) presented regional geological syntheses of the Pilbara Craton.

Based on lead isotope model ages that generally fall into two groups (*ca*. 3430–3370 and *ca.* 2950–2890 Ma), Huston *et al.* (2002b) suggested that orogenic lode-gold mineralization in the Pilbara Craton occurred during two episodes. Gold mineralization at the Zakanaka deposit, located 11 km south–southwest of the McPhees deposit, was dated at 2888 ± 6 Ma using a Pb–Pb isochron for three phases of alteration (Neumayr *et al.* 1998). Baker *et al.* (2002) correlated the structural timing of mineralization in the East Strelley Belt and suggested that the *ca.* 2890 Ma age applies to all gold deposits of the belt.

The northern part of this belt has a history of gold mining that began in the early 1930s (Finucane 1935). Large-scale production from the belt only occurred during the period 1994–1998 when 3.5 tonnes Au (average grade of 1.85 g/t Au) was extracted from five open-pit mines (Breccia Hill, Iron Stirrup, Main Hill, McPhees and Zakanaka; Fig. 1b).

Mineralization and Alteration

Gold mineralization and associated hydrothermal minerals are spatially associated with, and hosted within, D_5 shear zones at the McPhees deposit. A syndeformation timing of mineralization is suggested by planar hydrothermal veins that overprint equivalent, but folded (D_5) veins. The D_5 structures formed late in the complex structural evolution of the East Strelley Belt (Baker 2003), which involved an early, regional fabric-forming event (D_2) and two folding events (D_3 and D_4). At the McPhees mine, gold-related veins and alteration phases overprint several earlier structures including S_2, S_3 and S_4 fabrics. Generally, gold mineralization at the McPhees mine is distributed in elongate metabasaltic boudins surrounded by ultramafic schist that formed during D_2 shear-zone development (Baker *et al.* 2002). The boudins and, locally, the ultramafic schist are hydrothermally altered and are cut by gold-bearing actinolite – pyrrhotite ± talc ± carbonate ± quartz ± albite ± tourmaline veins. The highest-grade ore was mined from boudins that contain up to 50% actinolite–pyrrhotite veins with intervening albite- and tourmaline-altered wallrock. Gold generally occurs as fine (5–10 μm) grains within acicular vein actinolite or, more rarely, as small grains disseminated in composite grains of arsenopyrite overprinting ultramafic schist outside, but proximal to, the boudins.

Quartz in veins at the McPhees deposit is generally rare. However, of the alteration phases present, quartz is the most suitable mineral for a study of fluid inclusions. Therefore, in order to link quartz to the gold mineralizing event, intergrown quartz–actinolite and vein quartz containing radiating clusters of actinolite were selected for this study.

Fluid Inclusions

Petrographic examination and microthermometric analysis of fluid inclusions in quartz from auriferous veins were undertaken to determine the fluid-circulation history of the deposit and the composition of fluids responsible for gold mineralization. The following abbreviations for the thermometric data are used in this paper: T_mCO_2: temperature of melting of CO_2-rich phase, T_e: temperature of eutectic (first recognized melting), $T_m$ice: temperature of final melting of ice; T_mh: temperature of melting of hydrohalite, $T_m$clath: temperature of melting of CO_2 clathrate, T_hCO_2 (L or V): temperature of homogenization of liquid and vapor CO_2 phases to liquid or vapor, $T_h$tot (L or V): temperature of total homogenization to liquid or vapor, $T_m$dms: temperature of dissolution of solid phases, and T_d: temperature of decrepitation of inclusions.

Petrography of host quartz and inclusions

Quartz-vein material shows variable degrees of deformation and preservation of fluid inclusions. Typically, samples comprise quartz that is clear and relatively inclusion-free. However, most samples contain millimeter-scale regions with abundant and diverse types of fluid inclusions and minor evidence of strain (*e.g.*, undulatory extinction, subgrains). Clear regions in quartz are likely to represent recrystallized areas in the host grain, whereas the inclusion-rich and partly deformed regions are considered to represent non-recrystallized vein material. Inclusions hosted in this "early" quartz are the focus of this study, since the objective is to determine the composition of gold-bearing fluids. In selecting fluid-inclusion assemblages for thermometric study from regions of non-recrystallized quartz, only assemblages distal to both grain boundaries and planar arrays of secondary inclusions were selected. Figure 2 schematically illustrates the overprinting relations of the various types of inclusions described below and shows their different relations to the two types of quartz.

The early quartz preserves not only more inclusions (Fig. 3c), but also more diverse types and generations of inclusions than the clear quartz. Optically, the inclusions fall into three groups according to the number of phases at room temperature (~21°C) and to the spatial distribution of inclusions within assemblages (*e.g.*, inclusions located along planar, healed microfractures *versus* randomly distributed inclusions). Within early quartz, all three types of inclusions are preserved, whereas recrystallized quartz lacks Type-I inclusions.

Type-I inclusions (Figs. 3a, b) are two- or three-phase, CO_2-bearing (carbonic) inclusions that contain 0–90% aqueous liquid. At room temperature, two-phase inclusions contain liquid and vapor CO_2, whereas three-phase inclusions have an additional phase of aqueous liquid surrounding the CO_2. Typically, these inclusions have an equant to irregular morphology, and range from 8 to 15 μm in longest dimension; however, many larger (up to 35 μm) inclusions are present. Type-I inclusions typically occur as random three-dimensional clusters, and more rarely as discontinuous planar arrays that are confined to single crystals (*i.e.*, not cross-cutting grain boundaries). Type-I fluid inclusions are subdivided according to the degree of fill (F), defined as the volume of aqueous phase divided by the total volume of an inclusion. Type-Ia inclusions have F = 0 (no aqueous liquid visible), and Type-Ib inclusions have F > 0 (aqueous phase clearly visible). Typically, F values for Type-Ib inclusions are 0.02–0.10 (*i.e.*, 2–10% aqueous liquid by volume), but for some, they are as high as 0.90. These visual estimates were based on standard charts for regular inclusions (Shepherd *et al.* 1985); since this method is hindered by inclusion shape, however, some error is inevitable. Moreover, the optical limitations of microscopes hinder recognition of minor amounts of the aque-

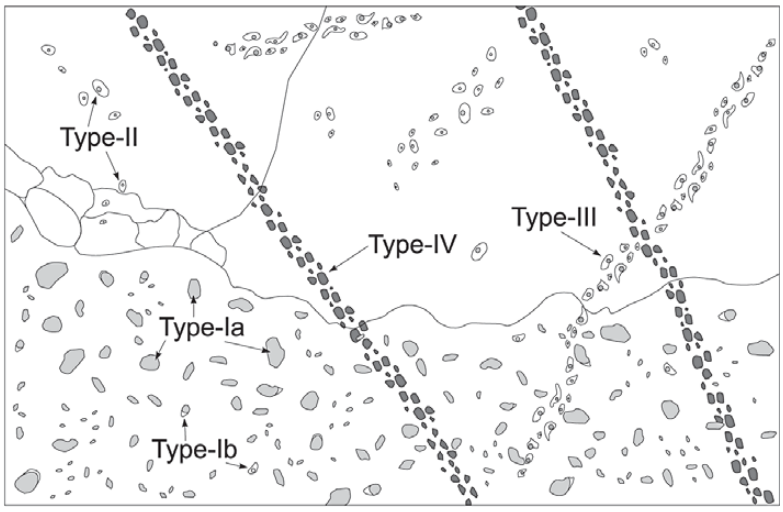

FIG. 2. Schematic sketch of the quartz veins from McPhees. Clear, recrystallized quartz (upper half) lacks Type-Ia (light gray) and Type-Ib (light gray + colorless aqueous phase) inclusions, whereas these CO_2-rich inclusions are abundant in unrecrystallized quartz (lower half). Type-II and -III aqueous inclusions (colorless aqueous phase plus grey water vapor phase) are younger and cut both types of quartz. Type-IV gas-rich inclusions (dark gray) cut both types of quartz and all other inclusions. Width of sketch is ~3 mm (the inclusions are not drawn to scale).

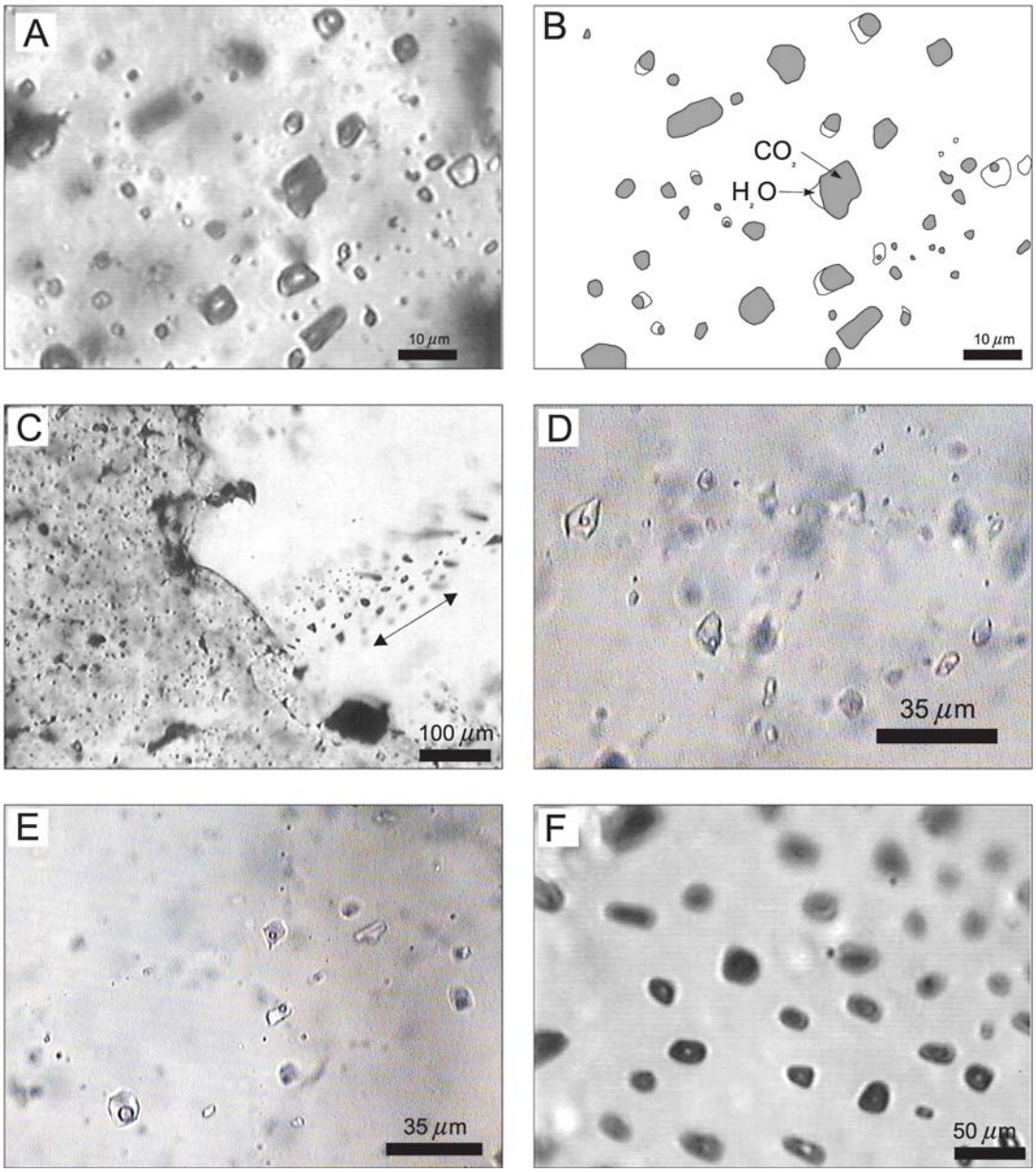

FIG. 3. Photomicrographs of fluid inclusions in quartz veins at the McPhees deposit. A. Typical Type-I fluid inclusion assemblage showing coexisting H_2O-rich and CO_2-rich fluid inclusions. B. Line sketch of inclusions shown in (A). C. Recrystallized quartz vein material (upper-right half) in association with millimeter-scale regions of non-recrystallized quartz that contain abundant, primary fluid inclusions (lower-left half). Healed microfracture containing late secondary, Type-IV fluid inclusions cuts both types of quartz (parallel to arrow). D. Three healed microfractures containing Type-II, high-salinity H_2O-rich fluid inclusions. E. Type-III, low-salinity aqueous fluid inclusions. F. Gas-rich Type-III secondary fluid inclusions.

ous phase. Many Type-Ib inclusions have a small quantity of aqueous liquid (~5%) that is only visible because of re-entrants, or other irregularities along inclusion walls. Roedder (1984) noted that because the aqueous phase wets inclusion walls, an H_2O content of at least 20% by volume is required in a perfectly round, mixed $CO_2 + H_2O$ inclusion before the aqueous phase is visible. Thus, an aqueous phase may be present in rounded Type-Ia inclusions as a thin, invisible meniscus surrounding the CO_2 liquid phase.

Based on the criteria of Goldstein (2003), the origin of Type-Ia and -Ib inclusions is indeterminable. They cannot be directly linked with growth of quartz crystals and therefore cannot be unequivocally deemed primary. Nor do they consistently occur in planar arrays. Despite this fact, it is clear that Type-I inclusions are only preserved in the weakly deformed parts of the host quartz veins. As other types of inclusions occur in both types of quartz, Type-I inclusions contain the earliest fluid preserved by the veins at McPhees.

The second group of inclusions preserved are two-phase aqueous inclusions that are morphologically similar, but contain two distinctly different compositions of fluid (high- and low-salinity), as determined from microthermometric analyses (see below). As such, they are divided into Type II and Type III and are discussed separately in subsequent sections. They typically occur in weakly to well-defined planar arrays that cut recrystallized quartz (Figs. 3d, e) and are, therefore, secondary inclusions. Rare Type-II inclusions and ~40% of Type-III inclusions contain a blocky, highly birefringent daughter mineral. All inclusions of Type II and III are liquid-rich, with a narrow range of F values (0.8–0.95) that is invariably more consistent within single assemblages. These inclusions typically have ellipsoidal to negative shapes and are 2–10 μm in longest dimension.

Type-IV inclusions (Fig. 3f) are monophase vapor-rich (mixed CO_2–N_2–CH_4) inclusions. They invariably occur as very distinct, planar arrays that cross-cut quartz grain-boundaries. Single planar arrays of these inclusions can be tracked for several millimeters across some thin sections. These inclusions typically have a negative morphology and a consistent size (4–10 μm). We were able to examine only CO_2-dominated Type-IV inclusions using standard thermometric procedures, whereas laser Raman spectroscopy provided information on the composition of N_2-and CH_4-rich inclusions. All Type-IV fluid inclusions are considered to represent the latest generation of secondary inclusions, as planar arrays of Type-IV inclusions cut planes of inclusions of Types II and III.

Microthermometric Results

The procedures and techniques followed for microthermometry are described in Appendix A, and data for Types I–IV fluid inclusions are summarized in Table 1.

TABLE 1. SUMMARY OF MICROTHERMOMETRIC AND LASER RAMAN

Inclus. Type	T_mCO_2	$T_m$ice	$T_m$clath	T_hCO_2	$X_{CO2, vap}$	$X_{N2, vap}$	$X_{CH4, vap}$	$T_h$tot
Ia	–57.3 ± 0.7 (–60.6 to –56.6) n=90			19.6 ± 5.2 (7.3 to 29.0) n=76	97.4 ± 1.4 (95 to 100) n=13	0.2 (0 to 1) n=13	2.5 (0 to 5) n=13	
Ib	57.8 ± 1.3 (–61.5 to –56.6) n=91	5.5 ± 2.9 (–9.9 to –1.5) n=16	6.0 ± 2.4 (1.6 to 8.7) n=14	23.0 ± 4.9 (13.5 to 30.9) n=87	98 ± 2.3 (93 to 100) n=17	<1 (0 to 3) n=17	1.6 (0 to 7) n=17	350 ± 41 (280 to 410) n=10 [5*L*, 5*V*]
II		–3.5 ± 2.0 (–8.8 to –0.2) n=33						207 ± 60 (123 to 336) n=31 [31*L*]
III		–21.4 ± 1.0 (–22.7 to –18.0) n=35						143 ± 37 (85 to 276) n=32 [30*L*,1*V*]
IV	–57.4 ± 0.2 (–57.6 to –57.0) n=10				28 (0–85) n=11	48 (0–92) n=11	25 (3–58) n=11	

Data are given as mean ± 1σ standard deviation, range in parentheses ( ), number of measurements and number of inclusions that homogenized to liquid *L* and vapor *V* phases in brackets [ ]. Laser Raman results are given in mol%.

Composition of Type-I inclusions: mixed aqueous–carbonic fluids

Microthermometric measurements on Type-Ia and -Ib inclusions were indistinguishable between, or between those inclusions in isolated random three-dimensional arrays and those in discontinuous planar arrays. Values of T_mCO_2 for all Type-I inclusions range from –61.5° to –56.6°C (mean –57.5°C; Fig. 4a). Small quantities of other gas species (*i.e.*, N_2, CH_4) lower the melting point (–56.6°C) of pure CO_2 (Hollister & Burruss 1976, Touret 1982). Raman spectroscopic techniques were applied to test for other gas species in Type-I inclusions. These results are presented below.

Although clathrate crystals are notoriously difficult to observe (Roedder 1984), $T_m$clath data were obtained for 14 Type-Ib inclusions using the criteria for clathrate detection of Collins (1979). Especially useful is the observation of double-freezing upon supercooling of these inclusions. This allowed $T_m$clath to be determined in the absence of ice, thus eliminating the problem of discriminating solid phases as either ice or clathrate. $T_m$clath data range from 1.6 to 8.7°C (mean 6.0°C; Table 1), which indicate salinities of 2.6 to 12.6 eq. wt.% NaCl using the equations of state of Bowers & Helgeson (1983) for inclusions with a pure CO_2 phase and of Kerrick & Jacobs (1981) for inclusions containing an impure CO_2 phase (Fig. 4b). Values of $T_m$ice for Type-Ib inclusions range from –9.9 to –1.5°C (mean –5.5°C; Table 1).

Composition of Type-II inclusions: moderate-salinity aqueous fluids

Type-II inclusions have temperatures of first melting (T_e; Fig. 5a) that range from –22 to –16°C. Final temperatures of ice melting ($T_m$ice) range from –8.8 to –0.2°C (Fig. 5b) and indicate salinities of 1 to 12 eq. wt.% NaCl (Bodnar 1993).

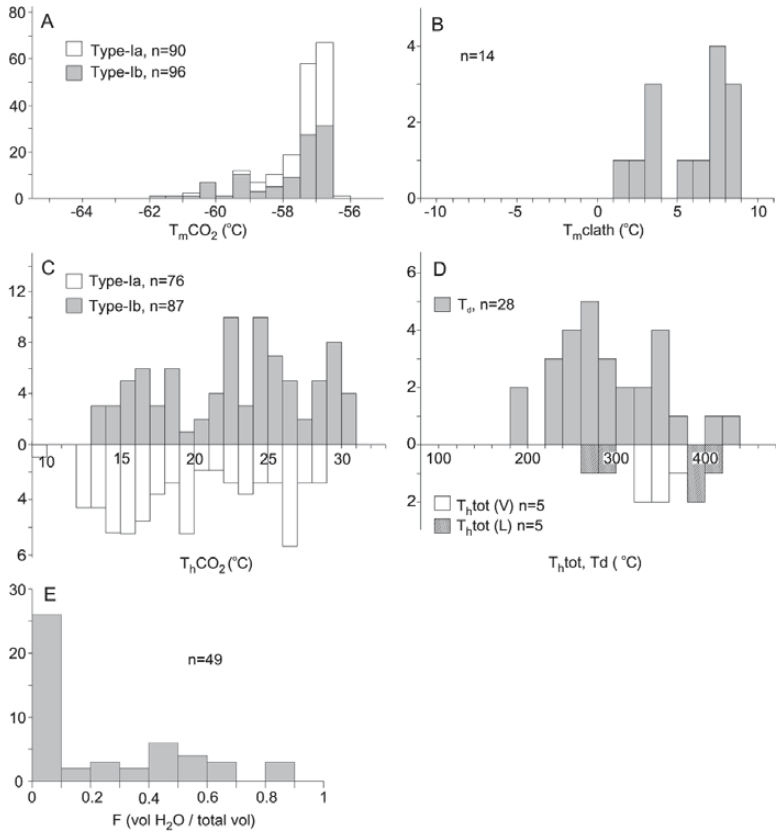

FIG. 4. Summary of freezing and heating thermometric data for Type-I (carbonic–aqueous) fluid inclusions from samples of gold-bearing quartz veins from the McPhees mine.

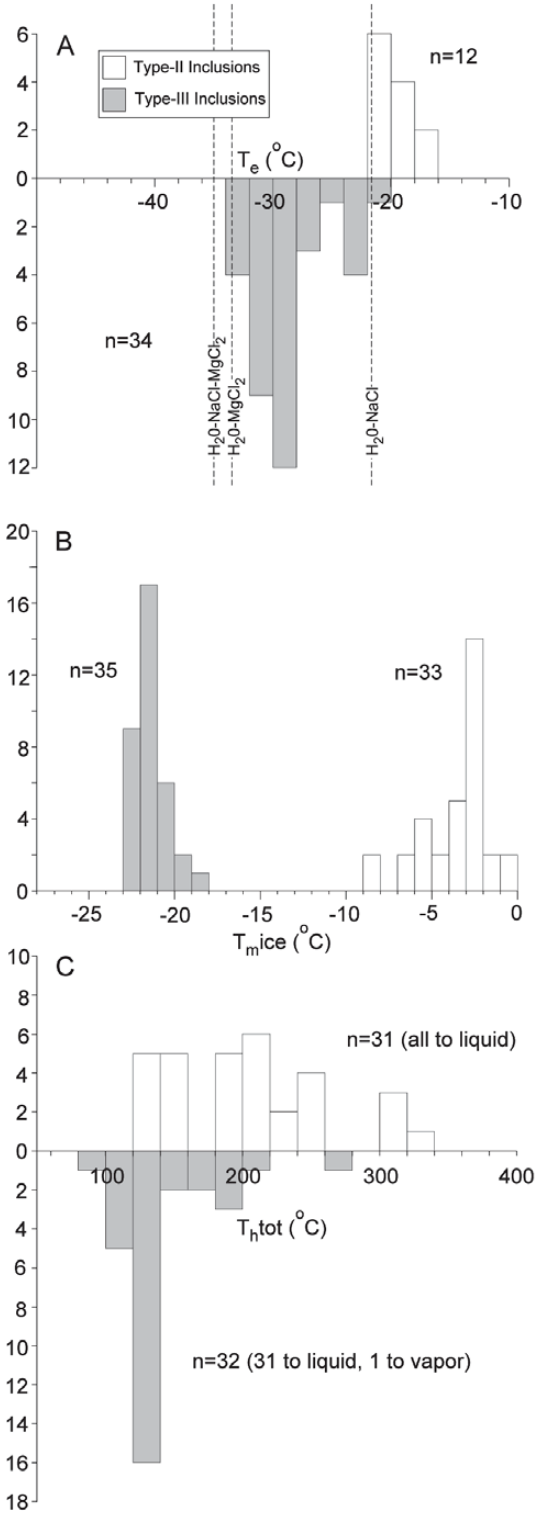

Composition of Type-III inclusions: high-salinity aqueous fluids

Type-III inclusions have $T_m$ice values that range from –22.7 to –18.0°C (Fig. 5b); they indicate salinities of 22.5–21.0 eq. wt.% NaCl (Bodnar 1993). Relative to Type-II inclusions, Type-III inclusions have much lower temperatures of first melting (T_e; Fig. 5a), in the range from –34 to –25°C. A pure H_2O–NaCl system generally contains no aqueous liquid phase below the eutectic point of –20.8°C, although a metastable eutectic may occur at –28°C (Roedder 1984). Consistent eutectic melting below this temperature suggests the presence of other salts. Eutectics for the binary system H_2O–$MgCl_2$ and ternary system H_2O–NaCl–$MgCl_2$ occur at –33.6°C and –35.0°C, respectively (Crawford 1981). Eutectic melting in this temperature range suggests that Type-III inclusions may contain $MgCl_2$ as a solute. Laser Raman analysis of Type-III inclusions were conducted to confirm the inferred presence of multiple solutes (see below).

Despite the similar optical characteristics of Type-II and -III inclusions, they contain very different proportions of cations and, therefore, may represent separate fluid-circulation events.

Heating experiments

Temperatures of homogenization of the CO_2 liquid and vapor phases (T_hCO_2) below the CO_2 critical point of 31.1°C were measured for 163 Type-I inclusions, of which three homogenized to the vapor phase, six showed critical homogenization, and the rest homogenized to the liquid phase. Type-Ia and -Ib inclusions showed similar even distributions over the temperature range +12 to +31°C. The CO_2 phase in Type-Ia inclusions homogenized over the range 7.3 to 29.0°C with a mean value of 19.6 ± 65.2°C (1σ; n = 76), whereas CO_2 in Type-Ib inclusions homogenized over the range 13.5 to 30.9°C with a mean value of 23.0 ± 4.9°C (1σ; n = 87; Fig. 4c). Total homogenization ($T_h$tot) of aqueous and carbonic phases in Type-Ib inclusions was attempted on 38 inclusions; among these, only ten homogenized (five to the vapor phase and five to the liquid phase) before the temperature of decrepitation (T_d) was reached. These data occur over the temperature range of 280 to 410°C with a mean value of 350 ± 41°C (1σ; n = 10; Fig. 4d).

Temperatures of total homogenization ($T_h$tot) for 31 Type-II aqueous inclusions were measured and vary

FIG. 5. Summary of freezing and heating thermometric data for Type-II and -III (aqueous) fluid inclusions from samples of gold-bearing quartz veins from the McPhees mine. Vertical dashed lines in (A) indicate the temperatures for major H_2O–salt eutectics.

from 123 to 336°C with a mean value of 207 ± 60°C (1σ; n = 31; Fig. 5c). All Type-II inclusions homogenized to the liquid phase.

Values of $T_h$tot for 32 Type-III inclusions were measured and fall into the lower range of 85 to 276°C with a mean of 143 ± 37°C (1σ; n = 32; Fig. 4c). One Type-III inclusion homogenized to the vapor phase, and the rest homogenized to the liquid phase. The dissolution of daughter minerals occurred before total homogenization at temperatures ($T_m$dms) from 74 to 136°C.

Variations in $T_h$tot and T_d measurements within representative assemblages of fluid inclusions are shown in Figure 6 for inclusions of Types I to III. Generally, fluid-inclusion assemblages of all three types of inclusions show narrow ranges, 30 to 40°C, with some outlying measurements. Generally, the variation among the earlier Type-I inclusions is greater than in secondary Type-II and Type-III inclusions, suggesting that some modification of Type-I inclusions may have occurred after trapping.

Laser-Raman Spectroscopic Analysis of Inclusion Compositions

The laser Raman analytical procedures are described in Appendix A, and data are summarized in Table 1.

Results on gas-phase composition

The presence of other gaseous species dissolved within CO_2 results in depression of the melting temperature for pure CO_2 (–56.6°C), as described above. Raman analysis of 13 Type-Ia and 17 Type-Ib inclusions confirmed thermometric results indicative of the presence of other species. Results for both types of inclusions were indistinguishable, and together ranged from 93 to 100 mol.% CO_2, 0–3 mol.% N_2 and 0–7 mol.% CH_4 (Fig. 7a).

Eleven Type-IV inclusions from three different samples were analyzed by the Raman technique. These late inclusions also contain a mixture of CO_2–CH_4–N_2, but proportions of CH_4 and N_2 are much greater (Fig. 7b). These data appear to fall into two distinct groups, as mixtures of CO_2 and CH_4, and CH_4 and N_2. However, one assemblage (represented by square symbols in Fig. 7) indicates that proportions of the gases within a single healed fracture also can be highly variable.

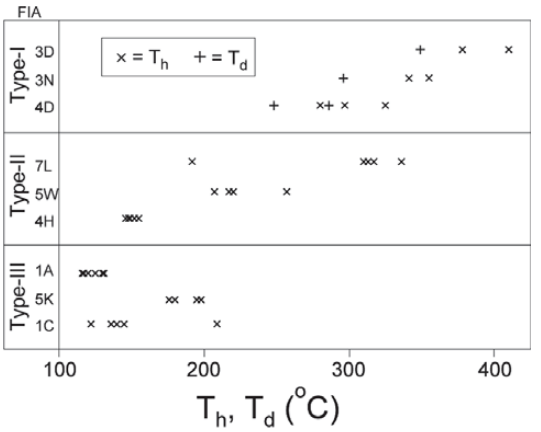

FIG. 6. $T_h$tot a°Cnd T_d measurements for selected assemblages of fluid inclusions of Types I to III. Laboratory identifiers and inclusion type are indicated to the left and individual measurements are plotted horizontally (x = T_h tot and + = T_d). The narrow range for each fluid-inclusion assemblage suggests that the inclusion assemblages did not undergo widespread post-entrapment modification.

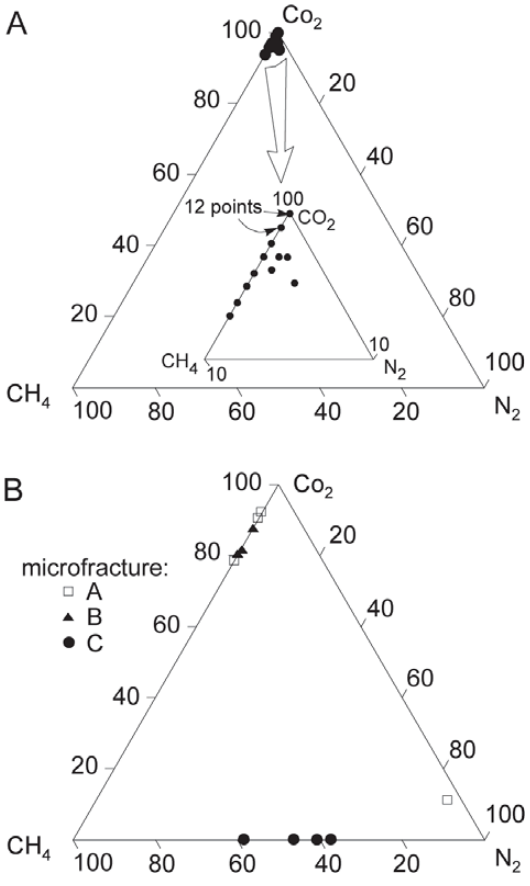

FIG. 7. Plots of results of laser-Raman analyses of gas-rich fluid inclusions. A. Type-I mixed carbonic-aqueous inclusions, showing the generally pure CO_2 content of these primary fluids. B. Analyses of inclusions from three healed microfractures containing secondary, Type-IV inclusions, showing the highly variable, gas-rich composition of these late fluids, even within a single healed microfracture.

Solute identification

Ten Type-III fluid inclusions were examined with the laser-Raman microprobe to identify mixed solutes indicated by the microthermometric investigations. The laser-Raman technique is incapable of identifying monatomic ions in solution at ambient temperatures because the instrument monitors characteristic Raman radiation emitted from vibrating covalent bonds. Supercooling of aqueous inclusions, however, causes ions to form covalently bonded hydrates that will emit Raman radiation (Dubessy *et al.* 1982). Addition of a Linkam MDS 600 heating–freezing stage to the system allowed inclusions to be cooled to –180°C during Raman analysis. The laser beam was then focused on darker, grainy areas that appeared to contain salt hydrates.

Typical Raman spectra display strong peaks characteristic of ice and $NaCl•2H_2O$ (hydrohalite). In addition, most spectra have one or more peaks characteristic of $MgCl_2•12H_2O$ hydrate, although this hydrate was only positively identified in one inclusion that gave spectral peaks at the 3396, 3464, 3478 and 3505 cm^{-1} (Dubessy *et al.* 1982). Type-III inclusions are, therefore, considered to contain a mixed salt composition of H_2O–NaCl–$MgCl_2$, which is consistent with the T_e values for those inclusions.

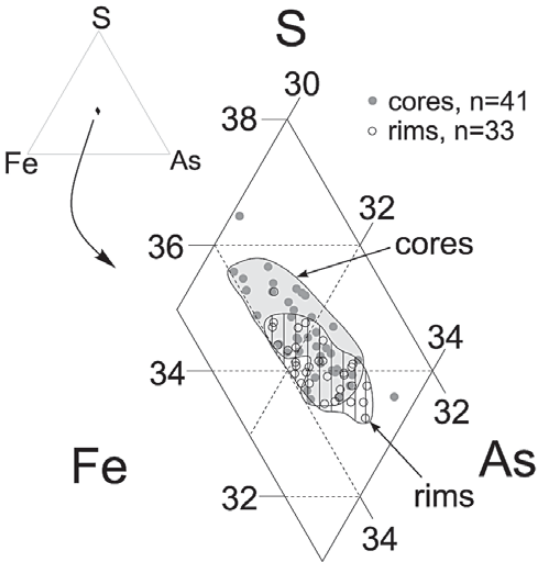

FIG. 8. Plot (atom %) of arsenopyrite from the McPhees deposit. Hollow circles represent spot analyses of rims, and dark grey circles represent analyses of grain cores. The shaded and vertically hatched regions represent the range of core and rim compositions, respectively (excluding three outliers), that were used to estimate temperatures of arsenopyrite growth (indicated in Fig. 9).

THE COMPOSITION OF ARSENOPYRITE

Arsenopyrite grains from three mineralized samples were examined. These grains are typically euhedral and isolated, but commonly occur in equilibrium with pyrrhotite in larger composite grains. A total of 97 individual chemical compositions were determined from 36 grains. Analytical procedures are described in Appendix A, and results of the analyses are shown in the As–Fe–S plot in Figure 8. The proportion of Fe ranges from 32.7 to 34.0 atomic %, which is similar to the stoichiometric value (33.3 atomic %). Proportions of sulfur are more variable, ranging from 33.3 to 36.5 atom %. The amount of As varies inversely with S and ranges from 30.1 to 33.7 atomic %. A wider spread of As and S values and enrichment in S relative to As are consistent with variations in the composition of arsenopyrite ($FeAs_{1-x}S_{1+x}$). In each sample analyzed, arsenopyrite occurs in textural equilibrium with pyrrhotite. Where S and Fe are buffered by a second sulfide phase, the proportion of As in arsenopyrite varies with temperature of deposition (Clark 1960, Barton 1969, Kretschmar & Scott 1976). Sharp *et al.* (1985) reviewed this geothermometer and determined that it is applicable to greenschist- and lower-amphibolite-grade deposits.

Results for the McPhees arsenopyrite show that, on average, the rim of individual grains contains ~0.3 atom % more As than the core. Kretschmar & Scott (1976) described similar zoning and attributed this effect to local fluctuations in $a(S_2)/a(As_2)$ related to growth kinetics of the grains. Thus, it may be inappropriate to view these data as related to temperature variations during growth. Furthermore, variation within grains was generally less than intergrain variations, so zoning is not assured. Compositions of the relatively As-rich rim suggest that growth occurred in the temperature range 360–460°C (using the average value with one outlying point removed), whereas compositions of the core suggest a lower range, 340–430°C (using the average value with two outlying points removed; Fig. 9). In a more conservative approach to the arsenopyrite thermometer, the complete range of As compositions (at 1σ standard deviation) from the McPhees deposit constrains the temperature of formation to ~300–480°C, regardless of possible compositional zonation (Fig. 9).

OXYGEN ISOTOPES

Oxygen isotopic measurements were made on four mineral pairs from vein-style ore samples from the McPhees deposit. Results for all analyses are presented in Table 2. Actinolite was analyzed in all four samples, and $\delta^{18}O$ values were found to range from +5.9 to +7.6‰. Coexisting quartz was analyzed in two samples of ore; $\delta^{18}O$ values range from +11.7 to +12.1‰. Albite and talc coexisting with actinolite were analyzed in the other two samples, and $\delta^{18}O$ values are +10.7‰ and +7.0 to +7.9‰, respectively.

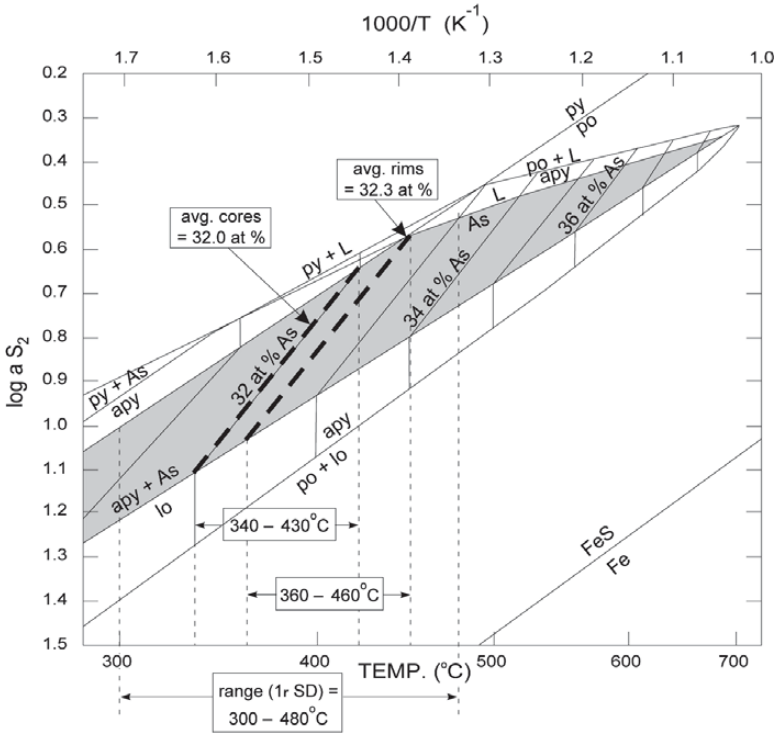

FIG. 9. Temperature – sulfur activity projection showing the stability field of arsenopyrite buffered by pyrrhotite. Isopleths indicate the atom % As in arsenopyrite. The average and range (1σ standard deviation) of values for arsenopyrite from McPhees is indicated and constrains the temperature of formation to <480°C. After Sharp *et al.* (1985).

TABLE 2. MEASURED OXYGEN ISOTOPIC COMPOSITIONS AND CALCULATED TEMPERATURES FOR VEIN MINERALS FROM THE MCPHEES DEPOSIT

Samp. #	Mineral $\delta^{18}O$ (‰/SMOW)				Temp. (°C)[1]	Error[2]
	quartz	actinolite	albite	talc		
152-97	+11.9	+6.2			341	+23 –21
	+11.7					
200-97	+11.7	+6.8			344	+32 –28
	+12.1	+5.9				
260-98		+6.7	+10.7		354	+39 –34
		+6.9				
309-98		+7.6		+7.9	~2500	
		+6.9		+7.0		

[1]Estimates for each sample calculated from the oxygen isotopic geothermometers of Zheng (1993a & b). Where multiple analyses exist, average values were used.
[2]Errors estimated by calculating Temp. using upper and lower limits at ±0.2‰ precision, or ±0.1‰ where duplicate analyses are very similar.

Using the quartz–actinolite, actinolite–albite and actinolite–talc oxygen isotope geothermometers of Zheng (1993a, b), these data provide estimates for the temperature of formation of these gold-associated hydrothermal minerals. Results (Table 2) indicate temperatures of 341°C (quartz–actinolite pair), 344°C (quartz–actinolite pair) and 354°C (actinolite–albite). Errors for these calculations were assessed using upper and lower limits of the precision of the isotopic determinations. All errors were less than ±40°C (Table 2). An unrealistic estimate of temperature of ~2500°C was obtained for an actinolite–talc pair and indicates isotopic disequilibrium. This sample contains abundant early talc, as well as the later hydrothermal talc that was targeted for this analysis, so a second possibility is that the $\delta^{18}O$ value of the sample is a mixed signature, influenced by the two generations of talc. Given the consistency of the temperature estimates, determined from the other three mineral pairs, ~350°C, those data best define the temperature of gold mineralization at the McPhees deposit. This temperature is consistent with the limited constraints (300–480°C) of the arsenopyrite thermometer.

Table 3 presents calculations of $\delta^{18}O$ isotopic compositions of fluid in equilibrium with the hydrothermal assemblages analyzed. We used the mineral–fluid fractionation factors of Clayton *et al.* (1972) for quartz, and those of Zheng (1993a, b) for quartz, actinolite and albite. All values fall in the narrow range of +6.0 to +7.5‰. The different fractionation-factors for quartz (Clayton *et al.* 1972, Zheng 1993a) provide results that differ by 0.2‰ only. This oxygen isotopic composition is similar to that in other late Archean orogenic gold deposits (Hodgson 1993), and is consistent with isotopic compositions of primary magmatic water (Sheppard 1986), water in equilibrium with arc and crustal felsic magmas (Taylor 1992, Hedenquist & Lowenstern 1994) and metamorphic water (Sheppard 1986, Taylor 1997). Thus, these data do little to constrain possible sources of fluid; however, the range of values is consistent with fluid interaction with a primitive source such as mafic volcanic rocks, consistent with the abundant mafic and ultramafic rocks within the East Strelley Belt.

Discussion

Type-I (CO_2–CH_4–H_2O–NaCl) fluid inclusions are abundant in unrecrystallized quartz from mineralized veins that are paragenetically and spatially associated with orebodies at the McPhees deposit. These inclusions are considered to be early and vein-related; given the close spatial association of veins with gold-related alteration phases (*e.g.*, actinolite), they are interpreted to contain fluids that transported gold. Typically, these inclusions are CO_2-rich, with no visible aqueous phase (although optical limitations of regularly shaped fluid inclusions require 20% aqueous liquid before this phase will be visible). Type-Ib inclusions contain various amounts of CO_2 [$X(CO_2)$ from 0.05 to 0.95; mean 0.5] and coexist with Type-Ia inclusions along the same discontinuous planes of fluid inclusions and in random assemblages in three dimensions. Therefore, although these inclusions have highly variable bulk-compositions, they probably have formed synchronously, and by the same mechanism.

TABLE 3. CALCULATED OXYGEN ISOTOPIC COMPOSITION OF MINERALIZING FLUIDS FROM THE MCPHEES DEPOSIT

Samp. #	Temp. (°C)	Mineral	Calc. $\delta^{18}O$ (‰/SMOW)	
152-97	341	quartz	+6.2[1]	+6.0[2]
		actinolite		+6.8[2]
200-97	344	quartz	+6.3[1]	+6.1[2]
		actinolite		+6.9[2]
260-98	354	actinolite		+7.5[2]
		albite		+7.5[2]

[1]fractionation factors of Clayton et al. (1972)
[2]fractionation factors of Zheng (1993a & b)

Origin of Type-I inclusions

Studies of fluid inclusions and mineral equilibria in orogenic gold-bearing systems have revealed that fluids responsible for these deposits are typically mixed, low-salinity (<~6 eq. wt.% NaCl) aqueous-carbonic fluids with $X(CO_2)$ in the range 0.05 to 0.25 (Colvine *et al.* 1988, Ho *et al.* 1990, Ridley & Diamond 2000). Thus, the dominance of CO_2-rich fluid inclusions at McPhees is atypical. However, CO_2-rich fluid inclusions can form by several mechanisms, including: (1) selective removal of H_2O from unmixed $CO_2 + H_2O$ fluids, (2) ductile, strain-induced leakage of H_2O from homogeneous CO_2–H_2O fluids, (3) selective trapping of vapor during phase separation of a homogeneous CO_2–H_2O fluid (see review by Hollister 1988), and (4) heterogeneous trapping of two fluids during mixing, which all can result in proximal trapping of H_2O- and CO_2-rich inclusions (Ramboz *et al.* 1982).

In a fluid inclusion containing unmixed $CO_2 + H_2O$, the aqueous phase wets the inclusion walls owing to the weakly polar nature of H_2O molecules (Watson & Brenan 1987). Thus, CO_2-rich fluid inclusions can form from post-entrapment leakage or necking of such inclusions, because the H_2O phase will be preferentially "wicked" from the inclusion (Crawford & Hollister 1986). The remaining CO_2 phase would expand to fill the inclusion, resulting in low-density, CO_2-rich inclusions. Huizenga & Touret (1999) suggested a comparison of CO_2 phase density with the volume percent aqueous liquid to test for selective leakage of H_2O. The CO_2 phase in CO_2-rich inclusions from McPhees tends to be denser than the CO_2 phase in H_2O-rich inclusions (Fig. 10), although this trend is based on a small proportion of low-density inclusions. Assuming a constant volume of the inclusions, the selective removal of H_2O from homogeneous or unmixed H_2O–CO_2 inclusions would result in the opposite effect. Thus, it seems unlikely that these CO_2-rich inclusions (and by implication the coexisting H_2O-rich inclusions) formed from secondary, post-entrapment processes. Furthermore, Type-I inclusions from McPhees do not show widespread indication of leakage or necking, despite partial recrystallization of the host quartz. Thus, these inclusions did not form by widespread removal of H_2O from inclusions that trapped a homogeneous H_2O–CO_2 fluid.

CO_2-rich fluid inclusions can also result from simultaneous trapping of immiscible fluids during phase separation. Slight changes in ambient physical conditions (*e.g.*, pressure) during the development of a shear zone can result in separation of CO_2-rich and H_2O-rich phases from a homogeneous H_2O–CO_2 fluid. Trapping of immiscible fluids will result in inclusion assemblages that have: (a) bimodal L:V ratios, and (b) coexisting vapor-rich inclusions that homogenize to vapor, and liquid-rich inclusions that homogenize to liquid over the same temperature range (Ramboz *et al.* 1982). Neither of these criteria is met by the McPhees inclusions: the L:V

ratios form a wide range of values, and although half of the Type-I inclusions homogenize to liquid and half to vapor (Fig. 4d), this pattern occurred over a wide range of temperature and without an obvious correlation between L:V ratio and homogenization behavior. Therefore, Type-Ia and Type-Ib inclusions cannot represent the liquid- and vapor-rich phases of an unmixed fluid, which rules out immiscibility as a possible explanation for these inclusions. Furthermore the scarcity of H_2O-rich inclusions relative to CO_2-rich inclusions indicates that they are not likely to be unmixed counterparts.

Heterogeneous trapping of two fluids is a fourth possible mechanism that can result in preservation of CO_2-rich fluid inclusions. Ramboz *et al.* (1982) outlined four criteria for determination of heterogeneous trapping of two fluids in the same inclusion: (1) simultaneous trapping of inclusions, (2) no evidence of leakage or necking, (3) very scattered degree of fill, $T_h$tot and bulk compositions, and (4) $T_h$tot histogram that is non-symmetrical and flattened. The McPhees Type-I inclusions meet the first two criteria, as described above. Figure 4 shows the scattered nature of the estimated degree of fill, the measured $T_h$tot and the calculated bulk compositions. Moreover, Figure 4d indicates the flattened distribution of $T_h$tot and T_d data for these inclusions. Heterogeneous trapping of two fluids requires that the fluids were either immiscible, or that they were slow to mix. Experimental studies indicate that fluids with very different densities will mix slowly (Henley & McNabb 1978). Therefore, inclusions with a range of compositions are expected, rather than inclusions of consistent intermediate composition (Shepherd *et al.* 1985).

Linear "mixing trends" on $T_h$tot *versus* eq. wt.% NaCl plots are commonly used to test for mixing of two fluids (Shepherd *et al.* 1985). Unfortunately, the combined difficulties in measuring $T_m$clath and of reaching total homogenization of the Type-Ib inclusions resulted in only two inclusions for which both $T_h$tot and salinity values are available, such that these inclusions remain untested on these grounds. However, this test implies that various amounts of the two end-member fluids were mixed to form *homogeneous*, hybrid fluids that then became trapped. In contrast, heterogeneous mechanical trapping of varying proportions of the two end-member fluids is likely to result in poorly defined mixing trends (Shepherd *et al.* 1985), so this test may not even constrain the McPhees inclusions.

Thus, we conclude, on the basis of the criteria of Ramboz *et al.* (1982), that our dataset is best explained by a process of heterogeneous trapping of fluids during gold mineralization and vein growth. The varied compositions of the fluid inclusions resulted from incorporation of various proportions of parent fluids. However, the mixing model is limited since the origin of the parent fluids is equivocal. Indeed, the most likely process to generate CO_2- and H_2O-rich parent fluids is phase separation. Thus, both fluid separation and mixing may have occurred at McPhees.

Conditions of gold deposition

Thermometric measurements on Type-Ia and -Ib fluid inclusions suggest that gold deposition occurred during mixing of the two fluids. Therefore, these inclusions have inherently variable bulk compositions and densities and only provide limited estimates on the composition of the gold-bearing fluid. In this section, we use these estimates, plus independent constraints (arsenopyrite geothermometry, oxygen-isotope thermometry and stratigraphic thickness) to constrain the temperature and depth (pressure) of mixing of the fluid media and deposition of gold at the McPhees deposit.

Figure 11 displays temperature estimates calculated from oxygen isotopic compositions and isochores inferred from bulk-density calculations based on thermometric data for Type-I fluid inclusions to derive P–T conditions for mineralization at the McPhees deposit. Most isochores fall within a field in which the total variation in pressure is about 1 kbar. Isochores calculated for a few Type-Ib fluid inclusions, however, plot as denser outliers. At the temperature of mineralization estimated from oxygen isotopes, pressures determined from all but six of the Type-Ib isochores are consistent within 1 kbar. The six outliers may represent slightly later fluids trapped while the system cooled. For a temperature near 350°C, the bulk of the isochores give pressures of about 1.0 to 2.0 kbar, a range that is in good agreement with estimates of pressure inferred from the

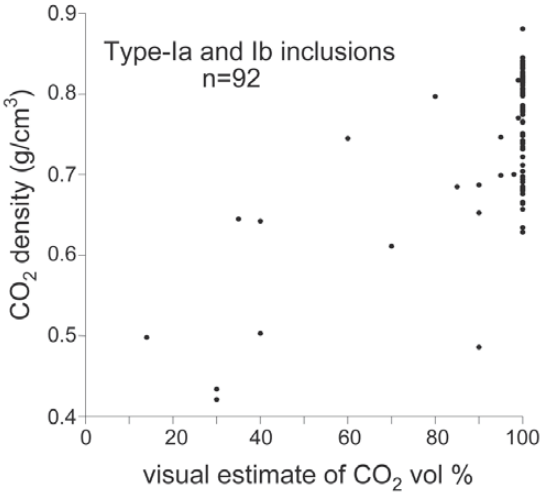

FIG. 10. Relation between CO_2 density and CO_2 proportion (based on visual estimate) for 93 Type-Ib fluid inclusions. Density was calculated from T_hCO_2 measurements. Inclusions with the densest CO_2 phase tend to have a smaller proportion of aqueous liquid.

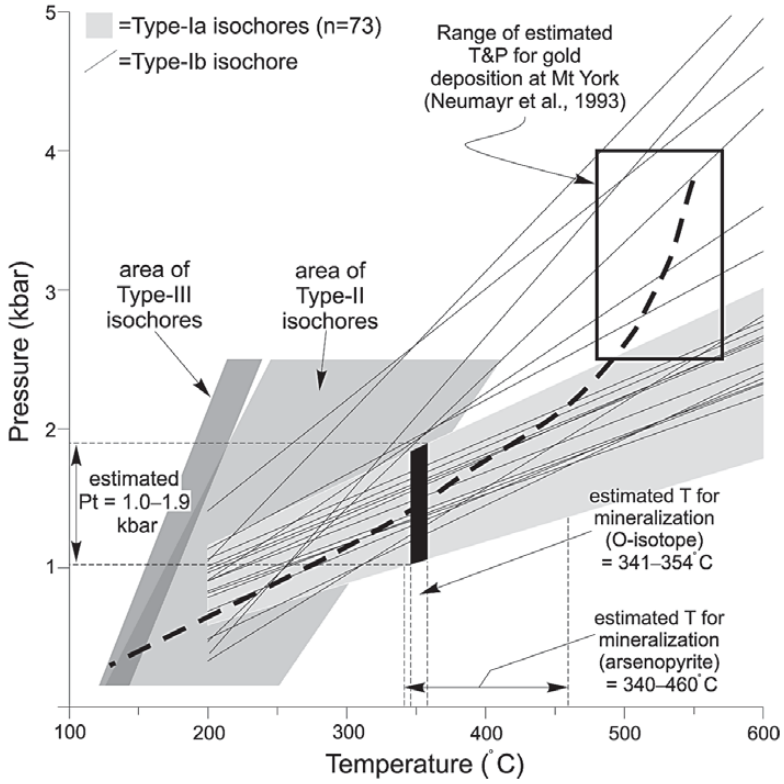

FIG. 11. Pressure–temperature plot showing isochores for Type-I, -II and -III fluid inclusions. Lightly shaded area contains 73 isochores for Type-Ia inclusions, and individual isochores (black lines) are shown for Type-Ib inclusions. Other shaded areas at lower T and P represent areas representing isochores for Type-II and Type-III inclusions. Isochores were calculated from microthermometric measurements using MacFlinCor software (Brown & Hagemann 1995). Vertical dashed lines indicate the estimated ranges for gold deposition from oxygen isotope and arsenopyrite thermometry, and the corresponding range in pressure. Conditions for gold deposition at the Mount York deposits are indicated by the outlined box. Heavy dashed line represents a possible path of fluid evolution for the East Strelley Belt.

thickness of the volcanic pile in the northern East Strelley Belt. The maximum thickness of supracrustal rocks is 7 km, which constrains the maximum pressure of formation of the McPhees deposit to about 2 kbar. Isochores for Type-II and Type-III fluids also are plotted on Figure 11. Although no independent estimates of temperature of trapping are available for these inclusions, they have lower $T_h$tot values, consistent with trapping during cooling and exhumation of the East Strelley Belt, rather than during gold mineralization.

Estimates on the temperature and pressure for gold mineralization at Mount York (Neumayr *et al.* 1993) indicate that, unlike at McPhees, gold was deposited under amphibolite-facies conditions (480–570°C and 2.5–4.0 kbar; box in Fig. 11). On the basis of structural timing, Baker *et al.* (2002) suggested that gold was deposited synchronously across the East Strelley Belt. Thus it appears that gold was deposited under a range of temperature and pressure conditions, which likely represents deposition at different levels in the crust. A potential pressure–temperature path is provided in Figure 11; given the ~11 km distance between the McPhees deposit and deposits at Mount York, however, it is unlikely that any part of the East Strelley Belt witnessed fluids moving along this entire path.

Variations in the density of primary, carbonic inclusion fluids are commonly encountered in fluid-inclusion studies of Archean orogenic gold deposits. In general, this phenomenon is attributed to fluctuating pressure on the fluid during mineralization (Robert & Kelly 1987,

Robert *et al.* 1995, Dugdale & Hagemann 2001). For large gold deposits with large systems of veins and alteration, such variations are a likely scenario, since multiple fluid-injection events and long-lived systems are responsible for gold deposition. However, the hydrothermal system at the McPhees deposit is small (0.4 t Au produced) relative to the world-class (>100 t Au) Archean lode-gold deposits, and evidence for large, long-lived fluid conduits is lacking. Furthermore, the talc schist surrounding metabasalt-hosted orebodies at McPhees would be more likely to promote diffuse flow of fluid owing to the low competency of the surrounding schist, rather than to sustain a conduit for strongly focused flow of fluid. Therefore, the density variations displayed by Type-I fluids (Fig. 11) are more easily explained by trapping variable proportions of the end-member fluids participating in mixing.

Secondary fluids

Fluid inclusions of Types II and III have similar appearances and both contain secondary fluids. Cross-cutting relations between these types of inclusions are ambiguous, but the salinity and minimum temperatures of trapping of these inclusions (Figs. 5b, c) distinguish them as being due to two separate fluid-circulation events. Type-II fluid inclusions have consistently higher minimum temperatures of trapping ($T_h$tot) and lower salinities than Type-III inclusions and are, therefore, interpreted to be earlier in the paragenesis, assuming a general trend toward cooler fluids in circulation. Type-II fluid inclusions have lower minimum temperatures of trapping than Type-I inclusions, consistent with the trapping of later, cooler fluids during thermal relaxation of the mineralizing system, or possibly of a very late fluid unrelated to mineralization (*e.g.*, Boullier *et al.* 1998). An aqueous, moderate-salinity fluid was trapped in Type-II inclusions, which typically occur in discontinuous planes that cut both primary and recrystallized quartz.

Type-III inclusions contain lower-temperature, highly saline brines composed of Na and Mg chlorides. As shown by Dubois & Marignac (1997), Mg-rich fluids may form by penetration of oceanic crust by seawater. However, Type-III inclusions are paragenetically late and were trapped after the occurrence of deformation, metamorphism and gold mineralization in the East Strelley Belt, and after stabilization of the Pilbara Craton. It is therefore unlikely that seawater could have played a role. High-Mg wallrock (deformed komatiite) is abundant in the McPhees area and represents an alternative, local source to explain the high Mg content of these fluids, which may originate from very late, retrograde metamorphism.

Type-IV fluid inclusions postdate all other inclusions and vein recrystallization, and occur in sharp continuous microfractures, more consistent with brittle deformation. These inclusions trap late fluids unrelated to gold mineralization.

Implications for mineralization

Most fluid-inclusion studies of orogenic gold deposits support gold transport by low-salinity aqueous fluids with low to moderate CO_2 content (see compilation by Ridley & Diamond 2000). However, CO_2-rich fluid with little or no H_2O component has been indicated as a primary, gold-depositing fluid (Schmidt Mumm *et al.* 1997, 1998), although the ability of such a fluid to transport gold has been questioned (Klemd 1998). A recent advance in modeling gold solubility at P–T conditions applicable to these deposits demonstrates that high solubility of gold can be maintained by gold–sulfide complexing in supercritical aqueous chloride fluids (Loucks & Mavrogenes 1999). Thus, the ability of a CO_2-dominated fluid to be an effective transporter of gold seems unlikely. Therefore, despite the abundant atypical primary CO_2 inclusions at McPhees, it is most likely that gold was transported by the aqueous component of these inclusions and deposition occurred during mixing with a CO_2-rich fluid. The origin of such a fluid remains equivocal, but it may have been derived from unmixing of a homogeneous CO_2–H_2O fluid in other parts of the hydrothermal system. Mixing of hydrothermal fluids will invariably cause changes in the ambient physicochemical conditions. Solubility of gold-sulfide complexes in hydrothermal fluids is sensitive to: (1) a decrease in H_2S content due to wallrock sulfidation (Neall & Phillips 1987), (2) a decrease in temperature (Loucks & Mavrogenes 1999), and (3) a decrease in pressure (Loucks & Mavrogenes 1999). Thus, fluid mixing is a potential mechanism of deposition for gold. Nonetheless, fluid mixing has rarely been identified as an important mechanism for gold deposition in Archean orogenic gold deposits (Hagemann & Cassidy 2000).

Two geological constraints have affected the distribution of ore at the McPhees deposit and have important implications for discriminating the mechanism of gold deposition. Firstly, ore is strongly localized in mafic lithologies, although halos of mostly disseminated mineralization occur in talc schist surrounding mafic boudins. Thus, a chemical control is implied for gold deposition. Secondly, the mafic boudins at McPhees have a much weaker pre-mineralization schistosity than the surrounding talc schist, and generally have a more competent mineralogy (an assemblage of actinolite – albite – chlorite in the mafic rocks *versus* talc – chlorite – carbonate in the talc schist). Deposit-scale mapping around the McPhees deposit (Baker *et al.* 2002) has shown that the foliation in the talc schist is deflected around mafic boudins, which are generally less deformed. In addition, hydrothermal veins are rare in the talc schist, but common in mafic boudins, suggesting that the less competent lithology was less prone to fracturing.

Loucks & Mavrogenes (1999) have shown that gold solubility in supercritical aqueous fluids (at similar conditions to those implied for McPhees) is extremely sensitive to decreases in T and P, whereas desulfidation of the fluid by reaction with Fe-rich wallrock (*e.g.*, the mafic boudins at McPhees) is of second-order importance. Thus, a decrease in pressure during fracturing of the mafic boudins and a decrease in temperature related to fluid mixing are likely to have played the largest roles in gold deposition.

Conclusions

1) Type-I fluid inclusions contain early, vein-related fluids that are dominantly CO_2-rich, with subordinate coexisting mixed carbonic-aqueous inclusions showing a highly variable L:V ratio. The high content of CO_2 in these inclusion fluids is atypical for orogenic lode-gold deposits.

2) Formation of these inclusions cannot be attributed to post-entrapment processes or to fluid immiscibility during inclusion trapping. The most likely mechanism involves fluid mixing and heterogeneous mechanical trapping. The CO_2-rich fluid could have been derived from phase separation in other parts of the hydrothermal system.

3) Parent fluids may be represented by the most CO_2-rich and most H_2O-rich inclusions. However, an infinite number of possible mixing trends exist, and these inclusions may also contain mixed fluids of intermediate composition.

4) Although fluid mixing can cause destabilization of gold complexes and gold deposition, the first-order control on gold deposition at McPhees was lithology, as evidenced by preferential mineralization of mafic rock.

5) Oxygen isotope geothermometers indicate that gold was deposited at ~350°C, corresponding to a pressure range of ~1–2 kbar (3.5–7 km), on the basis of calculated densities of the early vein-related fluid inclusions.

6) Calculated $\delta^{18}O$ isotopic compositions of the mineralizing fluid range from +6.0 to +7.5‰ and are consistent with fluid interaction with primitive volcanic rocks, such as the mafic and ultramafic sequences dominating the East Strelley Belt.

7) Secondary fluid inclusions contain aqueous fluids that record progressively lower temperatures and preserve higher-salinity fluids, suggesting entrapment of fluids during thermal relaxation and uplift.

8) The youngest fluid inclusions contain mixed gases (CO_2–CH_4–N_2).

Acknowledgements

This study forms part of a Ph.D. project by D.E.L.B., who acknowledges support of a University of Newcastle Postgraduate Research Scholarship and logistical support during 1997–98 by Lynas Gold N.L. Laser Raman analyses were conducted with the assistance of Terry Mernagh (Geoscience Australia), and oxygen isotopes analyses were conducted by Brad McDonald (CSIRO). Terry Mernagh provided insightful suggestions on an early version of the manuscript. Reviews by Steffen Hagemann, Daniel J. Kontak and Robert F. Martin greatly improved the paper.

References

Baker, D.E.L. (2003): *Gold Depositional Events and Their Relation to the Tectonic Evolution of the Pilbara Craton, Australia.* Ph.D. thesis, The University of Newcastle, Newcastle, Australia.

_____ & Seccombe, P.K. (2001): A possible magmatic component in Archaean gold mineralizing fluids at the McPhees mine, Pilgangoora Belt, Pilbara Craton, Western Australia. *Geol. Assoc. Can. – Mineral. Assoc. Can., Program Abstr.* **26**, 6.

_____, _____, & Collins, W.J. (2002): Structural setting and timing of gold mineralization in the northern East Strelley Belt, Pilbara Craton, Western Australia. *Econ. Geol.* **97**, 775-785.

Barley, M.E. (1993): Volcanic, sedimentary and tectonostratigraphic environments of the ~3.46 Ga Warrawoona Megasequence: a review. *Precamb. Res.* **60**, 47-67.

Barton, P.B., Jr. (1969): Thermochemical study of the system Fe–As–S. *Geochim. Cosmochim. Acta* **33**, 841-857.

Blewett, R.S., Huston, D.L., Mernagh, T.P. & Kamprad, J. (2002): The diverse structure of Archean lode gold deposits of the southwest Mosquito Creek Belt, east Pilbara Craton, Western Australia. *Econ. Geol.* **97**, 787-800.

Bodnar, R.J. (1993): Revised equation and table for determining the freezing point depression of H_2O–NaCl solutions. *Geochim. Cosmochim. Acta* **57**, 683-684.

Boullier, A.-M., Fridaous, K. & Robert, F. (1998): On the significance of aqueous fluid inclusions in gold-bearing quartz vein deposits from the southern Abitibi subprovince (Quebec, Canada). *Econ. Geol.* **93**, 216-223.

Bowers, T.S. & Helgeson, H.C. (1983): Calculation of the thermodynamic and geochemical consequences of nonideal mixing in the system $H_2O – CO_2 –$ NaCl on phase relations in geologic systems: equation of state for $H_2O – CO_2 –$ NaCl fluids at high pressures and temperatures. *Geochim. Cosmochim. Acta* **47**, 1247-1275.

Brown, P.E. & Hagemann, S.G. (1995): MacFlinCor and its application to fluids in Archean lode-gold deposits. *Geochim. Cosmochim. Acta* **59**, 3943-3952.

Card, K.D., Poulsen, K.H. & Robert, F. (1989): The Archaean Superior Province of the Canadian Shield and its lode gold deposits. *Econ. Geol., Monogr.* **6**, 19-36.

CLARK, L.A. (1960): The Fe–As–S system: phase relations and applications. *Econ. Geol.* **55**, 1345-1381, 1631-1652.

CLAYTON, R.N. & MAYEDA, T.K. (1963): The use of bromine pentafluoride in the extraction of oxygen from oxides and silicates for isotopic analysis. *Geochim. Cosmochim. Acta* **27**, 43-52.

_____, O'NEIL, J.R. & MAYEDA, T.K. (1972): Oxygen isotope exchange between quartz and water. *J. Geophys. Res.* **77**, 3057-3067.

COLLINS, P.L.F. (1979): Gas hydrates in CO_2-bearing fluid inclusions and the use of freezing data for estimation of salinity. *Econ. Geol.* **74**, 1435-1444.

COLVINE, A.C., FYON, J.A., HEATHER, K.B., MARMONT, S., SMITH, P.M. & TROOP, D.G. (1988): Archean lode gold deposits in Ontario. *Ont. Geol. Surv., Misc. Pap.* **139**.

CRAWFORD, M.L. (1981): Phase equilibria in aqueous fluid inclusions. *In* Short Course in Fluid Inclusions: Applications to Petrology (L.S. Hollister & M.L. Crawford, eds.). *Mineral. Assoc. Can., Short Course Handbook* **6**, 75-100.

_____ & HOLLISTER, L.S. (1986): Metamorphic fluids: the evidence from fluid inclusions. *In* Fluid–Rock Interactions During Metamorphism (J.V. Walter & B.S. Wood, eds.). Springer-Verlag, New York, N.Y. (1-35).

DUBESSY, J., AUDEOUD, D., WILKINS, R. & KOSZTOLANY, C. (1982): The use of the Raman microprobe mole in the determination of the electrolytes dissolved in the aqueous phase of fluid inclusions. *Chem. Geol.* **37**, 137-150.

DUBOIS, M. & MARIGNAC, C. (1997): The H_2O–NaCl–$MgCl_2$ ternary phase diagram with special application to fluid inclusion studies. *Econ. Geol.* **92**, 114-119.

DUGDALE, A.L. & HAGEMANN, S.G. (2001): The Bronzewing lode-gold deposit, Western Australia: P–T–X evidence for fluid immiscibility caused by cyclic decompression in gold-bearing quartz-veins. *Chem. Geol.* **173**, 59-90.

FINUCANE, K.J. (1935): McPhees Patch area, Pilbara Goldfield. *Aerial Geol. and Geophys. Surv. of N. Aust., W.A. Rep.* **1**.

GOLDFARB, R.J., GROVES, D.I. & GARDOLL, S.J. (2001): Orogenic gold and geologic time: a global synthesis. *Ore Geol. Rev.* **18**, 1-75.

GOLDSTEIN, R.H. (2003): Petrographic analysis of fluid inclusions. *In* Fluid Inclusions: Analysis and Interpretation (I. Samson, A. Anderson & D. Marshall, eds.). *Mineral. Assoc. Can., Short Course* **32**, 9-53.

_____ & REYNOLDS, T.J. (1994): *Systematics of Fluid Inclusions in Diagenetic Minerals*. Society of Economic Paleontologists and Mineralogists, Short Course **31**.

GROVES, D.I., KNOX-ROBINSON, C.M., HO, S.E. & ROCK, N.M.S. (1990): An overview of Archaean lode-gold deposits. *Geol. Dept Univ. Ext., Univ. Western Australia, Publ.* **20**, 2-18.

HAGEMANN, S.G. & CASSIDY, K.F. (2000): Archean orogenic lode gold deposits. *Rev. Econ. Geol.* **13**, 9-68.

HEDENQUIST, J.W. & LOWENSTERN, J.B. (1994): The role of magmas in the formation of hydrothermal ore deposits. *Nature* **370**, 519-527.

HENLEY, R.W. & MCNABB, A. (1978): Magmatic vapour plumes and ground-water interaction in porphyry copper emplacement. *Econ. Geol.* **73**, 1-20.

HICKMAN, A.H. (1983): Geology of the Pilbara Block and its environs. *Western Australia Geological Survey Bulletin* **127**.

HO, S.E., BENNETT, J.M., CASSIDY, K.F., HRONSKY, J.M.A., MIKUCKI, E.J. & SANG, J.H. (1990): Nature of ore fluid and transportational and depositional conditions in sub-amphibolite facies deposits. *Geol. Dept Univ. Ext., Univ. Western Australia, Publ.* **20**, 198-211.

HODGSON, C.J. (1993): Mesothermal lode-gold deposits. *In* Mineral Deposit Modeling (R.V. Kirkham, W.D. Sinclair, R.I. Thorpe & J.M. Duke, eds.). *Geol. Assoc. Can., Spec. Pap.* **40**, 635-678.

HOLLISTER, L.S. (1988): On the origin of CO_2-rich fluid inclusions in migmatites. *J. Metamorph. Geol.* **6**, 467-474.

_____ & BURRUSS, R.C. (1976): Phase equilibria in fluid inclusions from the Khtada Lake metamorphic complex. *Geochim. Cosmochim. Acta* **40**, 163-175.

HUIZENGA, J.M. & TOURET, J.L.R. (1999): Fluid inclusions in shear zones: the case for the Umwindsi shear zone in the Harare – Shamva – Bindura greenstone belt, NE Zimbabwe. *Eur. J. Mineral.* **11**, 1079-1090.

HUSTON, D.L., BLEWETT, R.S., KEILLOR, B., STANDING, J., SMITHIES, R.H., MARSHALL, A., MERNAGH, T.P. & KAMPRAD, J. (2002a): Lode gold and epithermal deposits of the Mallina Basin, north Pilbara Terrain, Western Australia. *Econ. Geol.* **97**, 801-818.

_____, _____, MERNAGH, T., SUN, S.-S. & KAMPRAD, J. (2001): Gold Deposits of the Pilbara Craton: Results of AGSO Research, 1998–2000, AGSO-Geoscience Australia Record 2001/10.

_____, SUN, S.-S., BLEWETT, R., HICKMAN, A., VAN KRANENDONK, M., PHILLIPS, D., BAKER, D. & BRAUHART, C. (2002b): The timing of mineralization in the Archean north Pilbara Terrain, Western Australia. *Econ. Geol.* **97**, 733-755.

KERRICH, D.M. & JACOBS, G.K. (1981): A modified Redlich–Kwong equation for H_2O, CO_2 and H_2O–CO_2 mixtures at elevated pressures and temperatures. *Am. J. Sci.* **281**, 735-767.

KLEMD, R. (1998): Comment on the paper by Schmidt-Mumm "High CO_2 content of fluid inclusions in gold mineralisations in the Ashanti Belt, Ghana: a new category of ore forming fluids?" (Mineralium Deposita 32: 107-118, 1997). *Mineral. Deposita* **33**, 317-319.

KRAPEZ, B. (1993): Sequence stratigraphy of the Archaean supracrustal belts of the Pilbara Block, Western Australia. *Precamb. Res.* **60**, 1-45.

KRETSCHMAR, R.S. & SCOTT, S.D. (1976): Phase relations involving arsenopyrite in the system Fe–As–S and their application. *Can. Mineral.* **14**, 364-386.

LOUCKS, R.R. & MAVROGENES, J.A. (1999): Gold solubility in supercritical hydrothermal brines measured in synthetic fluid inclusions. *Science* **284**, 2159-2163.

NEALL, F.B. & PHILLIPS, G.N. (1987): Fluid-wall rock interaction in an Archaean hydrothermal gold deposit: a thermodynamic model for the Hunt mine, Kambalda. *Econ. Geol.* **82**, 1679-1694.

NEUMAYR, P. (1993): *The Nature and Genesis of Archean, Syn-amphibolite Facies Gold Mineralisation in the Mt. York District, Pilbara Craton, Western Australia*. Ph.D. thesis, University of Western Australia, Nedlands, Australia.

_____, GROVES, D.I., RIDLEY, J.R. & KONING, C.D. (1993): Syn-amphibolite facies Archaean lode gold mineralisation in the Mt. York District, Pilbara Block, Western Australia. *Mineral. Deposita* **28**, 457-468.

_____, RIDLEY, J.R., MCNAUGHTON, N.J., KINNY, P.D., BARLEY, M.E. & GROVES, D.I. (1998): Timing of gold mineralization in the Mt York district, Pilgangoora greenstone belt, and implications for the tectonic and metamorphic evolution of an area linking the western and eastern Pilbara Craton. *Precamb. Res.* **88**, 249-265.

RAMBOZ, C., PICHAVANT, M. & WEISBROD, A. (1982): Fluid immisibility in natural processes: use and misuse of fluid inclusion data. II. Interpretation of fluid inclusion data in terms of immiscibility. *Chem. Geol.* **37**, 29-48.

RIDLEY, J.R. & DIAMOND, L.W. (2000): Fluid chemistry of orogenic lode gold deposits and implications for genetic models. *Rev. Econ. Geol.* **13**, 141-162.

ROBERT, F., BOULLIER, A.-M. & FIRDAOUS, K. (1995): Gold–quartz veins in metamorphic terranes and their bearing on the role of fluids in faulting. *J. Geophys. Res.* **100**, 12861-12879.

_____ & KELLY, W.C. (1987): Ore-forming fluids in Archean gold-bearing quartz veins at the Sigma mine, Abitibi Greenstone Belt, Quebec, Canada. *Econ. Geol.* **82**, 1464-1482.

_____ & POULSEN, K.H. (1997): World-class Archaean gold deposits in Canada: an overview. *Aust. J. Earth Sci.* **44**, 329-351.

ROEDDER, E. (1984): Fluid Inclusions. *Rev. Mineral.* **12**.

SCHMIDT MUMM, A., OBERTHÜR, T., VETTER, U. & BLENKINSOP, T.G. (1997): High CO_2 content of fluid inclusions in gold mineralisations in the Ashanti Belt, Ghana: a new category of ore forming fluids? *Mineral. Deposita* **32**, 107-118.

_____, _____, _____ & _____ (1998): High CO_2 content of fluid inclusions in gold mineralisations in the Ashanti Belt, Ghana: a new category of ore forming fluids? – a reply. *Mineral. Deposita* **33**, 320-322.

SHARP, Z.D., ESSENE, E.J. & KELLY, W.C. (1985): A re-examination of the arsenopyrite geothermometer: pressure considerations and applications to natural assemblages. *Can. Mineral.* **23**, 517-534.

SHEPHERD, T.J., RANKIN, A.H. & ALDERTON, D.H.M. (1985): *A Practical Guide to Fluid Inclusion Studies*, Blackie & Son Limited, Glasgow, U.K.

SHEPPARD, S.M.F. (1986): Characterization and isotopic variations in natural waters. *In* Stable Isotopes in High Temperature Geological Processes (J.W. Valley, H.P. Taylor, Jr. & J.R. O'Neil, eds.). *Rev. Mineral.* **16**, 165-184.

TAYLOR, B.E. (1992): Degassing of H_2O from rhyolitic magma during eruption and shallow intrusion, and the isotopic composition of magmatic water in hydrothermal systems. *Geol. Surv. Japan, Rep.* **279**, 190-194.

TAYLOR, H.P., Jr. (1997): Oxygen and hydrogen isotope relationships in hydrothermal mineral deposits. *In* Geochemistry of Hydrothermal Ore Deposits (H.L. Barnes, ed.). John Wiley and Sons, New York, N.Y. (229-302).

TOURET, J. (1982): An empirical phase diagram for a part of the N_2–CO_2 system at low temperatures. *Chem. Geol.* **37**, 49-58.

VAN KRANENDONK, M.J., HICKMAN, A.H., SMITHIES, R.H., NELSON, D.R. & PIKE, G. (2002): Geology and tectonic evolution of the Archaean North Pilbara Terrain, Pilbara Craton, Western Australia. *Econ. Geol.,* **97**, 695-732.

WATSON, E.B. & BRENAN, J.M. (1987): Fluids in the lithosphere. 1. Experimentally-determined wetting characteristics of CO_2–H_2O fluids and their implications for fluid transport, host-rock physical properties, and fluid inclusion formation. *Earth Planet. Sci. Lett.* **85**, 497-515.

WOPENKA, B. & PASTERIS, J.D. (1987): Raman intensities and detection limits of geochemically relevant gas mixtures for a laser Raman microprobe. *Anal. Chem.* **59**, 2165-2170.

ZHENG, Y.-F. (1993a): Calculation of oxygen isotope fractionation in anhydrous silicate minerals. *Geochim. Cosmochim. Acta* **57**, 1079-1091.

_____ (1993b): Calculation of oxygen isotope fractionation in hydroxyl-bearing silicates. *Earth Planet. Sci. Lett.* **120**, 247-263.

Received December 20, 2002, revised manuscript accepted March 8, 2004.

APPENDIX A: ANALYTICAL PROCEDURES

Fluid-inclusion thermometry

Vein samples were mostly collected after mine blasts from high-grade orebodies in McPhees north and south pits, or from piles of ore samples. Thus, most of the veins were not observed *in situ*. Despite this, the veins were constrained structurally and paragenetically by mine-scale mapping, which showed that similar styles of alteration (*i.e.*, coarse actinolite) and veins contain gold and are abundant within orebodies (Baker *et al.* 2002). Twelve selected samples were prepared as doubly-polished sections 60 μm thick, of which five sections were found to contain inclusions suitable for thermometric analyses. Standard petrographic investigation of selected samples was conducted to determine the paragenesis of host quartz and of the fluid-inclusion assemblages (Goldstein & Reynolds 1994). Before conducting freezing and heating experiments, locations of individual assemblages of fluid inclusions selected for further study were recorded, and these inclusions were described in terms of the number and type of phases at room temperature, inclusion size and shape, and their spatial distribution. Freezing experiments were carried out first, followed by heating, to avoid destroying sample chips by decrepitation. All inclusions for which freezing data were obtained were subsequently heated.

Freezing and heating experiments were performed using a Fluid Inc. adapted USGS-type gas-flow heating–freezing stage (Reynolds stage) mounted on a Leitz LABORLUX S microscope equipped with a 50× objective. Calibration against synthetic standards with phase changes at –56.6°C, –21.2°C, 0°C and +374.1°C was made prior to data collection. Commonly quoted limits of precision attainable on similar heating–freezing equipment are ±0.1°C and ±1.0°C for low-and high-temperature phase changes, respectively. Within this study, however, cycling methods were used to attain a minimum precision of ±1°C and ±5°C for low- and high-temperature measurements, respectively, since these levels of precision are geologically meaningful and allowed collection of significantly more data. An exception is the melting temperature (T_m) of CO_2, which was attained with a precision of ±0.1°C using slower rates of heating, since minor depression of this melting point indicates the presence of other gas phases (Hollister & Burruss 1976, Touret 1982). Raw thermometric data were reduced using the computer program MacFlinCor (Brown & Hagemann 1995) to determine density and compositional values.

For reconnaissance purposes, fluid inclusions were initially supercooled to –120°C and rapidly (~100°C per minute) warmed to approximately 30°C. This technique allows subtle phase-changes to be observed, since solid phases melt rapidly, with sudden motion that is more easily detected. The approximate temperature at which these changes occurred was noted, and a second supercooling with subsequent warming at ~1–2°C per minute in the range of previously observed phase-changes was then conducted to record the temperature of any observable phase-change. These slow heating runs were generally repeated several times for each inclusion until a precision of 1°C was attained for phase changes. During warming, emphasis was placed on observation of CO_2 melting (T_mCO_2) in the temperature range –65° to –56.6°C, final melting of ice ($T_m$ice), gas-clathrate melting ($T_m$clath) and CO_2 homogenization (T_hCO_2). Where observed, temperatures of the eutectic (T_e) and of melting of the salt hydrate (T_mh) also were recorded.

Laser Raman

Analysis of inclusions at the laser-Raman microprobe facility at Geoscience Australia, in Canberra, provided information on gas phase and solute composition for inclusions of Types I, III and IV. Laser-Raman spectra of fluid inclusions were recorded on a Dilor® SuperLabram spectrometer equipped with a holographic notch filter, 600 and 1800 g/mm gratings, and a liquid N_2 cooled 2000 × 450 pixel CCD detector. The inclusions were illuminated with 514.5 nm laser excitation from a Spectra Physics model 2017 argon ion laser, using 5 mW power at the samples, and a single 30-s accumulation. A 100× Olympus microscope objective was used to focus the laser beam and collect the scattered light. The focused laser spot on the samples measured approximately 1 μm in diameter. Wavenumbers are accurate to ±1 cm^{-1} as determined by plasma and neon emission lines. For the analysis of CO_2, O_2, N_2, H_2S and CH_4 in the vapor phase, spectra were recorded from 1000 to 3800 cm^{-1} using a single 20-s integration time per spectrum. The detection limits are dependent upon the instrumental sensitivity, the partial pressure of each gas, and the optical quality of each fluid inclusion. Raman detection limits (Wopenka & Pasteris 1987) are estimated to be about 0.1 mol.% for CO_2, O_2 and N_2, and 0.03 mol.% for H_2S and CH_4. Errors in the calculated ratios of gaseous species are generally less than 1 mol.%.

The composition of arsenopyrite

Arsenopyrite grains were analyzed with a JEOL JSM–840 scanning electron microscope at the University of Newcastle. Kretschmar & Scott (1976) recommended using an arsenopyrite standard for analyses in which As is sought. We used pure arsenic metal, however, as Sharp *et al.* (1985) found comparable results using both types of standards. The grains were analyzed

using an accelerating voltage of 20 kV and a beam current of 150 μA for 60 seconds. Rims and cores of each grain were analyzed separately to test for internal zonation. Nearly 25 percent of the datasets were discarded owing to analytical totals outside the accepted range of 98–101% (Kretschmar & Scott 1976). Grains were analyzed for As, S, Fe, Bi, Co, Ni and Sb, but only the first three elements were detected.

Oxygen isotopes

Representative samples of veins were examined by standard microscopic methods, and intimately intergrown pairs of minerals that showed no reaction textures (suggesting mineral disequilibrium) were selected. An effort was made to select mineral pairs from samples containing fluid inclusions suitable for microthermometric measurement. Two samples (152–97 and 200–97) met these criteria. Minerals were separated under a binocular microscope by partly crushing veins and then hand-picking, or by micro-drilling. Following mineral separation, concentrates were tested for contamination using temporary mounts containing >1000 grains each. These were examined with a standard petrographic microscope. All concentrates were found to contain only trace amounts of contaminants (0–10 grains per mount), except the albite fraction of sample 260–98, which contained about 0.5% actinolite.

Analyses of the minerals for their oxygen isotope compositions were undertaken at the Centre for Isotope Studies, the Commonwealth Scientific and Industrial Research Organisation (CSIRO), North Ryde, Australia, according to conventional procedures using BrF_5 (Clayton & Mayeda 1963). Isotopic ratios of the resulting CO_2 gas were measured on a Finnigan MAT252 mass spectrometer, relative to an internal standard that has been calibrated relative to SMOW. Precision is estimated to be ±0.2‰ (1σ), based on long-term analyses of standards. Duplicate analyses (conducted on six of eight concentrates) were found to be within 0.9‰ of each other (average 0.57‰).